Calculated energy loss of swift He, Li, B, and N ions in SiO_2, Al_2O_3, and ZrO_2

Santiago Heredia-Avalos and Rafael Garcia-Molina
Departamento de Física, Universidad de Murcia, Apartado 4021, E-30080 Murcia, Spain

José M. Fernández-Varea
Facultat de Física (ECM), Universitat de Barcelona, Diagonal 647, E-08028 Barcelona, Spain

Isabel Abril
Departament de Física Aplicada, Universitat d'Alacant, Apartat 99, E-03080 Alacant, Spain
(Received 16 March 2005; published 4 November 2005)

We have calculated the electronic stopping power and the energy-loss straggling parameter of swift He, Li, B, and N ions moving through several oxides, namely SiO_2, Al_2O_3, and ZrO_2. The evaluation of these stopping magnitudes was done in the framework of the dielectric formalism. The target properties are described by means of a combination of Mermin-type energy-loss functions that characterize the response of valence-band electrons, together with generalized oscillator strengths to take into account the ionization of inner-shell electrons. We have considered the different charge states that the projectile can have, as a result of electron capture and loss processes, during its motion through the target. The electron density for each charge state was described using the Brandt-Kitagawa statistical model and, for He and Li ions, also hydrogenic orbitals. This procedure provides a realistic representation of both the excitation properties of the target electrons and the projectile charge density, yielding stopping powers that compare reasonably well with available experimental data above a few tens of keV/amu.

DOI: 10.1103/PhysRevA.72.052902 PACS number(s): 34.50.Bw, 77.22.−d, 47.27.Vf, 61.46.+w

I. INTRODUCTION

The energy deposition by fast ions in chemical compounds, such as oxides, is a topic of special interest due to its multiple technological applications [1]. A precise knowledge of the stopping power and the energy-loss straggling parameter is important for the processing of semiconductors by ion-beam implantation as well as in the structural characterization of solids by ion-beam methods [2]. Recent experiments provide accurate determinations of the stopping powers of some oxides using foil transmission or backscattering techniques [3–8]. On the other hand, theoretical calculations of these stopping magnitudes are rather scarce [8,9].

In this work we calculate the stopping power and the energy-loss straggling parameter for swift He, Li, B, and N ions moving through various oxides, namely SiO_2, Al_2O_3, and ZrO_2. The considered projectile energies range from 10 to 5000 keV/amu, thus covering the important energy region around the stopping power maximum. We have chosen SiO_2 and Al_2O_3 as targets because they are relevant materials in microelectronic devices, and their stopping powers have been measured for He and N ions [3–6,8,10,11]; on the other hand, ZrO_2 is a high dielectric-constant compound with possible applications in microelectronics [12]. The stopping magnitudes are obtained employing the dielectric formalism, with a practical and realistic description of both the electronic excitation spectra of the solids and the projectile charge density. Similar calculations for H ions in these oxides were carried out and reported previously [9].

This paper is organized as follows. In Sec. II we introduce the model adopted in our calculations; a presentation of the results and a comparison with the available experimental data is made in Sec. III. Finally, the conclusions are given in Sec. IV. Atomic units are used throughout this work except where otherwise stated.

II. THEORETICAL MODEL

Let us consider a projectile with atomic number Z_1 and mass M_1 moving with nonrelativistic velocity v (kinetic energy $E=\frac{1}{2}M_1v^2$) through a solid. In the energy range of present concern, the nuclear stopping power can be safely neglected [13]. We evaluate the electronic stopping power $S(v)$, which gives the average energy loss per unit path length, as the weighted sum of the stopping powers for the different charge states q that the projectile can acquire during its travel through the target, that is,

$$S(v)=\sum_{q=0}^{Z_1}\phi_q(v)S_q(v). \tag{1}$$

Here ϕ_q is the fraction of the charge state q and S_q is the corresponding stopping power at the velocity v; the sum extends over all possible charge states q of the projectile. Notice that the contributions to S due to electron capture and loss as well as to projectile excitation are disregarded. Analogously, the energy-loss straggling parameter Ω^2, which represents the mean square deviation per unit path length of the energy-loss distribution, is given by

$$\Omega^2(v)=\sum_{q=0}^{Z_1}\phi_q(v)\Omega_q^2(v), \tag{2}$$

where Ω_q^2 corresponds to the straggling parameter of the solid when the ion charge state is q.

We calculate the velocity-dependent electronic stopping power S_q for a given charge state q of the projectile within the framework of the dielectric formalism, which assumes a linear response of the medium to the external perturbation produced by the passing ion [14],

$$S_q(v) = \frac{2}{\pi v^2}\int_0^\infty dk\,\frac{\rho_q^2(k)}{k}\int_0^{kv} d\omega\,\omega\,\mathrm{Im}\left[\frac{-1}{\epsilon(k,\omega)}\right], \quad (3)$$

where k and ω are the momentum and energy transferred to the excitations of the target electrons, respectively; $\rho_q(k)$ is the Fourier transform of the projectile charge density for the charge state q, and $\mathrm{Im}[-1/\epsilon(k,\omega)]$ is the energy-loss function (ELF) of the traversed medium, which takes into account its response to external perturbations. Similarly, the velocity-dependent energy-loss straggling parameter Ω_q^2 can be evaluated by means of the expression

$$\Omega_q^2(v) = \frac{2}{\pi v^2}\int_0^\infty dk\,\frac{\rho_q^2(k)}{k}\int_0^{kv} d\omega\,\omega^2\,\mathrm{Im}\left[\frac{-1}{\epsilon(k,\omega)}\right]. \quad (4)$$

It is worth mentioning that the contributions to S_q and Ω_q^2 due to the polarization of the projectile charge cloud are for He, Li, B, and N ions much smaller than in the case of H ions [15], and have therefore been neglected.

A. Charge fractions

In order to evaluate the charge fractions ϕ_q for ions with $Z_1 \geqslant 3$, we assume that they are proportional to the Gaussian charge-state distribution

$$f_q = \frac{1}{\sqrt{2\pi d^2}}\exp\left[-\frac{(q-\langle q\rangle)^2}{2d^2}\right], \quad (5)$$

where $\langle q\rangle$ and d are the mean (i.e., the equilibrium charge) and the standard deviation of the distribution, respectively. Both $\langle q\rangle$ and d are taken from a recent fit to experimental data [16,17] and depend on Z_1, v and the target atomic number Z_2. As the charge fractions ϕ_q must satisfy the normalization condition $\Sigma_{q=0}^{Z_1}\phi_q = 1$, they can be evaluated through the expression

$$\phi_q = \frac{f_q}{\sum_{q=0}^{Z_1} f_q}. \quad (6)$$

For the particular case of He ions, the charge fractions are obtained by solving the following system of Eq. (17):

$$\sum_{q=0}^{Z_1}\phi_q = 1, \quad (7)$$

$$\sum_{q=0}^{Z_1} q\,\phi_q = \langle q\rangle, \quad (8)$$

$$\sum_{q=0}^{Z_1} q^2\,\phi_q = \langle q^2\rangle, \quad (9)$$

where $\langle q^2\rangle = d^2 + \langle q\rangle^2$.

B. Charge density of the projectile

A widely used representation of the charge density of the projectile is the statistical model proposed by Brandt and Kitagawa [18] (BK hereafter), in which the $N = Z_1 - q$ bound electrons are all characterized by a generic orbital. In this scheme the Fourier transform of the charge density is

$$\rho_q^{(\mathrm{BK})}(k) = Z_1 - \frac{N}{1+(k\Lambda)^2}, \quad (10)$$

where Λ is a variational parameter given by

$$\Lambda = \frac{0.48\,N^{2/3}}{Z_1 - N/7}. \quad (11)$$

However, in order to describe properly the radial electron density when $N = 1$ or 2 we use [19]

$$\Lambda = \frac{3}{2[Z_1 - 0.3(N-1)]}. \quad (12)$$

An alternative way to model the projectile-electron radial density $4\pi r^2\rho_e(r)$ when $N \leqslant 4$ consists of using $1s$ and $2s$ hydrogenic wave functions. The corresponding Fourier transform can be written as [14]

$$\begin{aligned}\rho_q^{(\mathrm{h})}(k) = Z_1 &- [N\Theta(2-N) + 2\Theta(N-2)] \\ &\times\left\{1+\left[\frac{k}{2Z'_{1,\mathrm{S}}(1s)}\right]^2\right\}^{-2} - 2(N-2)\Theta(N-2) \\ &\times\left\{\left[\frac{k}{Z'_{1,\mathrm{S}}(2s)}\right]^2 - 1\right\}\left\{\left[\frac{k}{Z'_{1,\mathrm{S}}(2s)}\right]^2 - \frac{1}{2}\right\} \\ &\times\left\{1+\left[\frac{k}{2Z'_{1,\mathrm{S}}(2s)}\right]^2\right\}^{-4}, \end{aligned} \quad (13)$$

where $\Theta(\cdots)$ is the Heaviside step function. The effective charges $Z'_{1,\mathrm{S}}$ account for the screening of the interaction between each projectile electron and the nucleus due to the presence of the other projectile electrons. Slater's rules [20] can be used to quantify this effect. The dynamic screening of the interaction by the target electrons originates a further reduction of the effective charges, denoted by the prime in $Z'_{1,\mathrm{S}}$ [15]; the labels $1s$ or $2s$ indicate that the effective nuclear charge is evaluated for the electron in the $1s$ or $2s$ orbital, respectively. As a consequence, $Z'_{1,\mathrm{S}}$ depends on the velocity of the ion. This model furnishes, in principle, a more accurate representation of $\rho_q(k)$ than the general treatment proposed by BK [18] when only a few electrons are bound to the projectile nucleus.

C. Energy-loss functions

The inelastic collisions that the projectile experiences with the target electrons can be suitably modelled in terms of the dielectric response function of the traversed medium, and consequently with its ELF. Within this formalism, it is important to properly incorporate the different response of the target's valence-band and inner-shell electrons to the perturbation induced by the projectile charge. We therefore assume that

$$\mathrm{Im}\left[\frac{-1}{\epsilon(k,\omega)}\right]=\mathrm{Im}\left[\frac{-1}{\epsilon(k,\omega)}\right]_{\mathrm{vb}}+\mathrm{Im}\left[\frac{-1}{\epsilon(k,\omega)}\right]_{\mathrm{is}}, \quad (14)$$

where $\mathrm{Im}[-1/\epsilon(k,\omega)]_{\mathrm{vb}}$ and $\mathrm{Im}[-1/\epsilon(k,\omega)]_{\mathrm{is}}$ are the contributions to the ELF due to the valence-band and inner-shell electrons, respectively.

The interaction between the projectile and the weakly bound valence-band electrons of the target is complicated due to the effect of chemical bonding and the existence of collective excitations. In order to obtain a reliable description of $\mathrm{Im}(-1/\epsilon)_{\mathrm{vb}}$ we have adopted a sum of Mermin-type ELFs, $\mathrm{Im}(-1/\epsilon_{\mathrm{M}})$ [21] to account for the excitations of these loosely bound electrons [22–24]. In this scheme, we determine $\mathrm{Im}(-1/\epsilon)_{\mathrm{vb}}$ in the optical limit (i.e., $k=0$) by means of a fit of the form

$$\mathrm{Im}\left[\frac{-1}{\epsilon(k=0,\omega)}\right]_{\mathrm{vb}}=\sum_i A_i\,\mathrm{Im}\left[\frac{-1}{\epsilon_{\mathrm{M}}(\omega_i,\gamma_i;k=0,\omega)}\right] \quad (15)$$

to the available experimental optical ELF, $\mathrm{Im}[-1/\epsilon(k=0,\omega)]_{\mathrm{exp}}$. In the above expression ω_i and γ_i are related to the position and width, respectively, of the ith Mermin-type ELF that appears in the experimental spectrum, while the A_i coefficient determines its relative weight. The optical ELF $\mathrm{Im}[-1/\epsilon(k=0,\omega)]_{\mathrm{vb}}$ is analytically extended to all values of wave number k through the properties of the Mermin dielectric function [23]. In brief, this procedure models all electronic excitations in the optical limit of the ELF and provides a consistent extension to the whole (k,ω) range. It is therefore expected to constitute a rather faithful representation of $\mathrm{Im}[-1/\epsilon(k,\omega)]_{\mathrm{vb}}$ for each particular target.

In turn, the tightly bound inner-shell electrons have relatively large binding energies, thus retaining a marked atomic character and displaying negligible collective effects. We can include the ionization of these electrons by having recourse to the generalized oscillator strengths (GOS) [25] of the inner shells of the atoms in the target material. Using the relation between the ELF and GOS [26], then $\mathrm{Im}[-1/\epsilon(k,\omega)]_{\mathrm{is}}$ for a compound $A_{\alpha_1}B_{\alpha_2}\ldots$ is given by

$$\mathrm{Im}\left[\frac{-1}{\epsilon(k,\omega)}\right]_{\mathrm{is}}=\frac{2\pi^2\mathcal{N}}{\omega}\sum_j \alpha_j\sum_{n\ell}\frac{df_{n\ell}^{(j)}(k,\omega)}{d\omega}, \quad (16)$$

where $\mathcal{N}$ is the molecular density of the target (molecules per unit volume) and $df_{n\ell}^{(j)}(k,\omega)/d\omega$ is the GOS of the (n,ℓ) subshell of the jth element. The sums extend over the inner shells of all the atoms in the compound. Of course, ionization of a given shell can only take place if the energy transfer ω is larger than the threshold energy $\omega_{n\ell}$. For the sake of simplicity, here we adopt hydrogenic GOSs instead of more cumbersome GOSs computed numerically; the analytical expressions of the hydrogenic GOSs for K, L, and M shells are reviewed in the Appendix. This approach yields reasonable values of the inner-shell ionization cross sections [27,28] except near the threshold, where these cross sections are small.

The experimental ELF in the optical limit should be known for a wide range of excitation energies to compare with, but for some compound targets, and especially for high-energy excitations, there are no measurements of the ELF. In these cases, we estimate the ELF of a compound target $A_{\alpha_1}B_{\alpha_2}\ldots$ from the ELFs of its elementary constituents, $\mathrm{Im}[-1/\epsilon(k,\omega)]_j$, applying the weighted additivity rule [9,29]

$$\mathrm{Im}\left[\frac{-1}{\epsilon(k,\omega)}\right]=\mathcal{N}\sum_j\frac{\alpha_j}{n_j}\,\mathrm{Im}\left[\frac{-1}{\epsilon(k,\omega)}\right]_j, \quad (17)$$

where n_j is the atomic density of the jth element. In order to calculate n_j, we use the densities given in Table I [30]. The ELF of each element, to be used within this method, can be obtained from the experimental x-ray scattering factors [31].

TABLE I. The parameters used in describing the ELF of SiO_2, Al_2O_3, and ZrO_2 for high energies [see Eq. (16) and the Appendix].

Element	Shell	$\hbar\omega_{n\ell}$ (eV)	$Z_{2,S}$
O (ρ=1.426 g/cm^3)	K	543.4	7.7
Al (ρ=2.7 g/cm^3)	K	1560	12.7
Si (ρ=2.33 g/cm^3)	K	1839	13.7
Zr (ρ=6.49 g/cm^3)	K	18005	39.7
	L	2313	35.85

We show in Fig. 1 the ELFs in the optical limit ($k=0$) of the three oxides studied in this paper (i.e., SiO_2, Al_2O_3, and ZrO_2) as a function of the excitation energy of the target electrons; for clarity purposes we plot the ELF for high excitation energies in separated insets. The solid curves represent our fitted ELFs; the symbols and the dashed curves denote experimental data, as explained in the caption of the figure. In Table II we present, for each oxide, the values of the parameters ω_i, γ_i, and A_i pertaining to the ith Mermin-type ELF in the target ELF arising from the excitations of the valence-band electrons; see Eq. (15) and Ref. [9]. Table I contains the values of $Z_{2,S}$ and the threshold energy $\omega_{n\ell}$ corresponding to the ELF for the inner-shell electrons [see Eq. (16) and the Appendix].

The L shells of Si and Al and the M shell of Zr are modelled using Mermin-type ELFs [21] instead of GOSs [25]. This is because such shells with intermediate binding energies are affected to a certain extent by the presence of neighbor atoms in the condensed system, and display some collective effects. Indeed, Fig. 1 shows that the experimental ELFs have a smooth dependence on ω around the corresponding ionization energies, in contrast to the sharp edges observed for the tightly bound K shells of Si and Al and the L shell of Zr. We have checked numerically this assumption, obtaining that the ELFs evaluated using GOSs, Eq. (16), to describe the L shells of Si and Al and the M shell of Zr do not agree with the experimental ELFs.

As mentioned above, the low-energy region of the target ELF was obtained through a fit to the experimental ELF for each compound, whereas for the higher excitation energies, where experimental data are scarce or do not exist, the ELF of the compound was evaluated from Eq. (16) and compared with the ELF obtained from experimental x-ray scattering factors [31] using the weighted sum of the ELF of its atomic

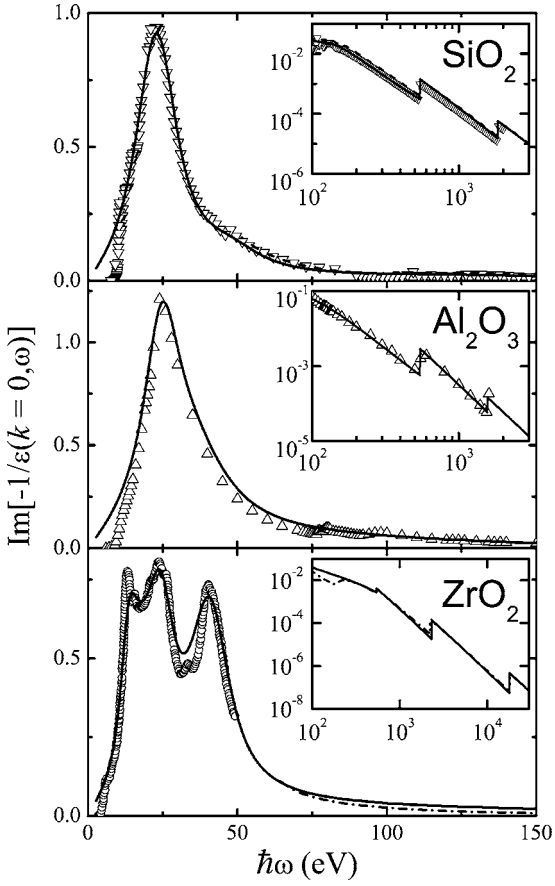

FIG. 1. The ELF in the optical limit ($k=0$) of SiO_2, Al_2O_3, and ZrO_2 as a function of the excitation energy. The solid curves represent our fit to the experimental ELF, which are denoted as follows. SiO_2: ▽, [32]; --, [33]. Al_2O_3: △, [34]; -·-, from x-ray scattering factors [31]. ZrO_2: ○, [35]; -·-, from x-ray scattering factors [31]. Notice that at high energies the ELF obtained from the x-ray scattering factors practically coincides with our calculated ELF.

constituents, Eq. (17). Note the continuity between the high-energy region of the ELF calculated from Eq. (16) and the low-energy region of the ELF obtained directly from the experimental data.

Besides reproducing the main features of the experimental ELF in the optical limit, the parameters used to fit the ELF were chosen in such a manner that the effective number of electrons per molecule participating in the electronic excitations up to a given energy ω,

$$N_{\mathrm{eff}}(\omega)=\frac{1}{2\pi^2\mathcal{N}}\int_0^{\omega}d\omega'\,\omega'\,\mathrm{Im}\left[\frac{-1}{\epsilon(k=0,\omega')}\right], \qquad (18)$$

tends to the number of electrons filling the orbitals of the target atoms. Of course, N_{eff} tends to the total number of electrons of the molecule when the excitation energy goes to infinity [9], i.e., the f-sum rule is fulfilled. We also checked our procedure to fit the ELF by calculating the mean excitation energy I of each compound, which only depends on the electronic structure of the target [36]

TABLE II. The parameters used to fit, through Eq. (15), the low-energy region of the ELF for SiO_2, Al_2O_3, and ZrO_2.

Target	i	$\hbar\omega_i$ (eV)	$\hbar\gamma_i$ (eV)	A_i
SiO_2	1	24.16	15.78	5.96×10^{-1}
($\rho=2.32$ g/cm^3)	2	48.98	27.21	4.63×10^{-2}
	3	136.05	125.17	1.60×10^{-2}
Al_2O_3	1	25.31	12.25	3.82×10^{-1}
($\rho=3.97$ g/cm^3)	2	35.37	32.65	4.44×10^{-1}
	3	100.68	136.05	5.11×10^{-2}
ZrO_2	1	13.06	2.72	8.03×10^{-2}
($\rho=5.6$ g/cm^3)	2	16.87	8.16	1.69×10^{-1}
	3	24.49	10.07	2.35×10^{-1}
	4	41.36	15.97	2.16×10^{-1}
	5	108.84	498.78	1.28×10^{-1}

$$\ln I=\frac{\displaystyle\int_0^{\infty}d\omega\;\omega\ln\omega\;\mathrm{Im}[-1/\epsilon(k=0,\omega)]}{\displaystyle\int_0^{\infty}d\omega\;\omega\;\mathrm{Im}[-1/\epsilon(k=0,\omega)]}. \qquad (19)$$

The mean excitation energy values resulting from this expression are $I(SiO_2)=137$ eV, $I(Al_2O_3)=145.3$ eV, and $I(ZrO_2)=312.8$ eV [9], in good accordance with the available experimental data {$I(SiO_2)=139.2$ eV and $I(Al_2O_3)=145.2$ eV [37]} and with the mean excitation energy obtained from Bragg's rule {$I(SiO_2)=141$ eV, $I(Al_2O_3)=143$ eV, and $I(ZrO_2)=295$ eV [38]}.

III. RESULTS AND DISCUSSION

Using Eqs. (1)–(4) with the previous representations of the ELF for SiO_2, Al_2O_3, and ZrO_2, the charge fractions from Refs. [16,17] and $\rho_q(k)$ from the BK and hydrogenic models, we have calculated the stopping power and energy-loss straggling parameter for the considered He, Li, B, and N dressed ions. A magnitude that is often used to quantify the energy loss per unit path length is the stopping cross section (SCS), which is defined as

$$\mathrm{SCS}(10^{-15}\ \mathrm{eV\ cm^2/molecule})=8.539\,\frac{S(\mathrm{a.u.})M_2(\mathrm{amu})}{\rho(\mathrm{g/cm^3})}, \qquad (20)$$

where M_2 and ρ are the atomic mass and the density of the target, respectively.

A. Stopping power for He ions

In Fig. 2 we show the SCSs of SiO_2, Al_2O_3, and ZrO_2 for He ions as a function of the projectile energy per atomic mass unit. The possible charge states that the He ion can acquire during its motion through the target are He^{2+}, He^{+}, and He^{0}. The solid curves correspond to the SCSs calculated using the modified BK model [18,19] for $\rho_q(k)$, Eq. (10),

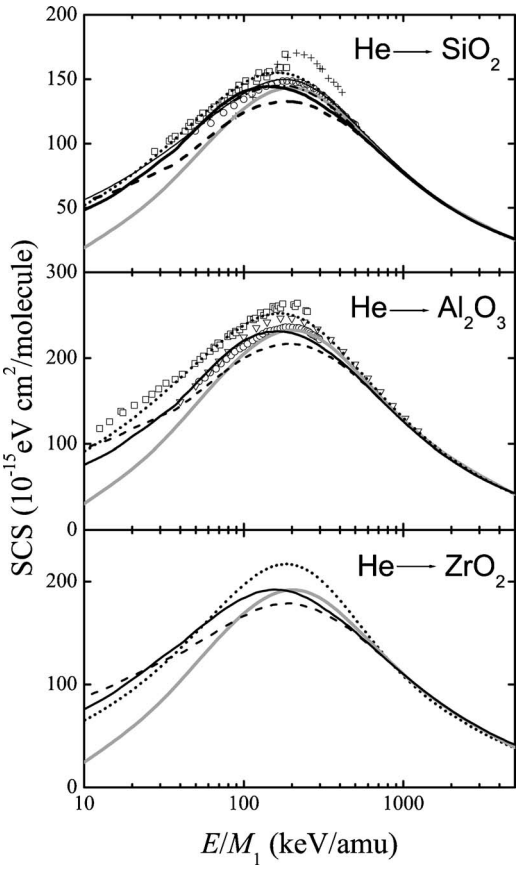

FIG. 2. The SCSs of SiO_2, Al_2O_3, and ZrO_2 for swift He ions as a function of their energy per atomic mass unit. The solid and dashed curves represent our calculations using $\rho_q^{(BK)}(k)$ and $\rho_q^{(h)}(k)$, respectively. The dotted curves correspond to the SRIM-2003 code [30], whereas the gray solid curves are the results obtained with the CasP program [39]. Symbols denote experimental measurements: + [10], ○ [11], □ [3], and ▽ [6]. The dash-dotted and thin solid curves, only for SiO_2, are the parametrized experimental data sets of Refs. [4,5], respectively.

whereas the dashed curves represent the SCSs when hydrogenic orbitals are employed, Eq. (13). Experimental data from various sources [3,6,10,11] are indicated by symbols, except the parametrized data sets for SiO_2 reported by Lennard *et al.* [4] and by Pascual-Izarra *et al.* [5], which are depicted as dash-dotted and thin solid curves, respectively. For comparison purposes, we have plotted as dotted curves the semiempirical predictions of the SRIM-2003 code [30], which are based on fits to experimental stopping powers, and as gray solid curves the results obtained through the unitary convolution approximation (UCA) implemented in the CasP program, including both target and projectile ionization and excitation [39]. The SCS calculations performed with the modified BK model show a satisfactory agreement with most of the available experimental data for SiO_2 and Al_2O_3 targets [3–6,11]. Contrary to what could be expected, the agreement between the SCSs evaluated with $\rho_q^{(h)}(k)$ and the experimental measurements is poorer. The largest discrepancies between both theoretical data sets appear at energies around and below the maximum of the SCS. For instance, the SCS of SiO_2 at $E/M_1 \sim 100$ keV/amu obtained with

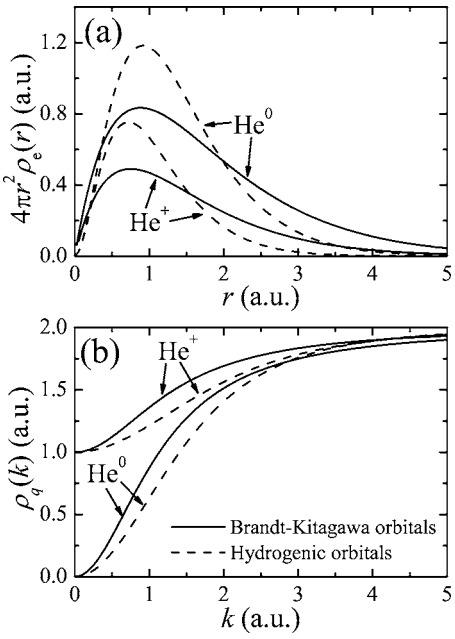

FIG. 3. (a) The radial electron density and (b) Fourier transform of the charge density of He^0 and He^+ ions moving through an amorphous SiO_2 target with $E/M_1 = 125$ keV/amu. The solid and dashed curves represent our calculations when the electron distribution is described by the modified BK model, Eqs. (10) and (12), or using hydrogenic orbitals, Eq. (13), respectively.

$\rho_q^{(h)}(k)$ is ~10% lower than the corresponding SCS when $\rho_q^{(BK)}(k)$ is used; this is due to the different descriptions of the electrons bound to the projectile, which are mainly present at low energies. However, at high energies ($\gtrsim$500 keV/amu), when the He atom is fully stripped of its electrons, both approaches obviously give identical results.

To better understand the origin of the observed differences between the SCSs calculated by means of the BK and hydrogenic models, Fig. 3 displays the radial electron density, and its respective $\rho_q(k)$ function, of He^0 and He^+ ions moving with $E/M_1 = 125$ keV/amu through an amorphous SiO_2 target. We can see that the electronic cloud of the projectile has a larger spatial extension when it is described by BK orbitals, leading to a larger "effective charge." This explains the higher SCSs if the BK model is used.

We recall that the contributions to the SCS due to electron capture and loss by the projectile as well as to the projectile excitation are not included in the present approach. The proposed estimate in Ref. [15] and the values reported in Ref. [40], both made for swift protons in aluminum, suggest that these processes could amount to ~10% near the SCS maximum. According to Fig. 2, the comparison between our two theoretical calculations and the experimental data would remain fairly good if electron capture and loss and projectile excitation effects were added to the SCSs. In fact, the improvement in the SCSs evaluated with $\rho_q^{(h)}(k)$ should be remarkable, bringing the results of this model into satisfactory agreement with experiment.

Unfortunately, there are no experimental SCSs of ZrO_2 to compare with. In any case, our SCSs agree reasonably well with the SRIM-2003 semiempirical results [30] at high ener-

gies and the largest discrepancies, observed at the maximum of the SCS, are smaller than 15%.

Note that, when there are not experimental SCS measurements for the compound target, the corresponding predictions by SRIM-2003 are obtained from the application of Bragg's rule to the SCS of the target constituents. The differences between the experimental SCS and the ones obtained from Bragg's rule are attributed to the chemical effect, i.e., the difference between the SCS of a compound compared to a mixture of its constituents [3]. Our calculations take into account the chemical effect because the fit of the low-energy region of the ELF to the experimental ELF of the compound target, but SRIM-2003 does not consider this effect [7]. So the main discrepancies between our results and the SRIM-2003 semiempirical predictions could be attributed to these chemical effects.

B. Stopping power for Li, B, and N ions

Calculations have also been performed for Li, B, and N ions moving through SiO_2, Al_2O_3, and ZrO_2 targets, and the corresponding SCSs are plotted in Fig. 4 as a function of the energy per atomic mass unit. The solid curves are our results when $\rho_q^{(\mathrm{BK})}(k)$ is used to model the projectile charge density. SCSs predicted by the SRIM-2003 code [30] are indicated as dotted curves. Symbols are experimental SCSs for N ions. In addition, for the N ions too, we have depicted the results obtained using the CasP program [39] as gray solid curves and the SCSs calculated using the density functional theory (DFT) [8] as thin solid straight lines. In the case of Li ions the dashed curves are theoretical SCSs obtained with $\rho_q^{(\mathrm{h})}(k)$.

Although there is a clear disagreement between the calculated SCSs of SiO_2 and Al_2O_3 for N ions and the available experimental data, which is more important as the projectile energy decreases, our results link reasonably well with the experimental values when the projectile energy increases ($E/M_1 \gtrsim 40$ keV/amu). These discrepancies between theory and experiment mainly appear because the dielectric formalism assumes a linear response of the target electrons to the perturbation induced by the ion's charge, which loses validity at low energies. In addition, energy losses due to both projectile excitation and electron capture and loss are not included in our calculations, as previously stated. But whereas such processes enhance the SCS values, nonlinear (i.e., nonperturbative) effects reduce them; as a consequence, these two contributions to the SCS, which are significant at low and intermediate projectile energies, compensate each other to a large extent [39].

Even though the dielectric formalism is valid for a wide range of projectile energies, depending on its atomic number (covering a wider energy interval as Z_1 decreases), it is not applicable for low energies; in this case the more elaborate DFT should be used. The binary theory proposed in Ref. [41] and the UCA described in Ref. [39] could be used for higher energies.

As expected, the differences between our results and the SRIM-2003 semiempirical values for intermediate and high energies increase with Z_1 because nonlinear effects, which are more important for heavier projectiles, are not included in our calculations. On the other hand, the chemical effect on the SCS, to be considered in compound targets [3,9], is not incorporated in the SRIM-2003 predictions [7] and increases with Z_1, because the SCS is proportional to Z_1^2 when the projectile is fully stripped of its electrons, i.e., for large projectile energies.

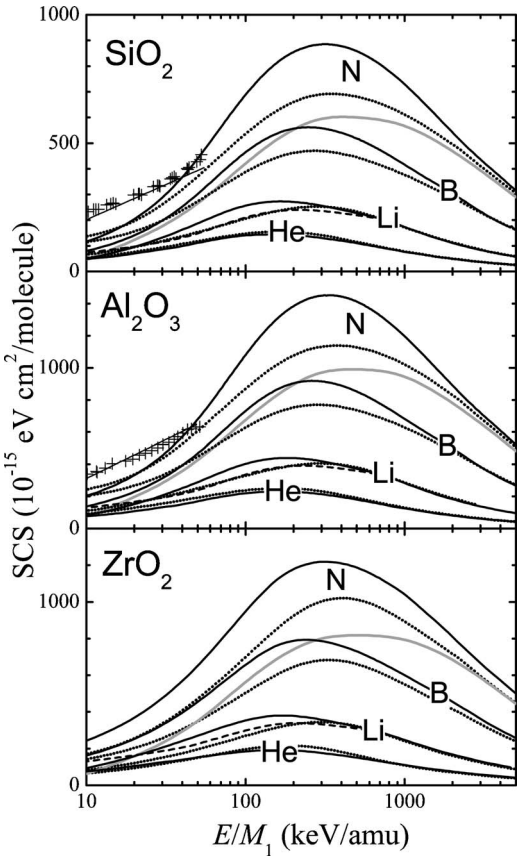

FIG. 4. The SCSs of SiO_2, Al_2O_3, and ZrO_2 for swift He, Li, B, and N ions as a function of their energy per atomic mass unit. The solid curves represent our calculations with $\rho_q^{(\mathrm{BK})}(k)$, whereas the dashed curves (only for Li) indicate the results when $\rho_q^{(\mathrm{h})}(k)$ is used. The dotted curves correspond to SRIM-2003 semiempirical calculations [30]. Symbols are the experimental SCSs for N projectiles; the thin solid lines and the gray solid curves are the corresponding SCSs calculations using the DFT [8] and the CasP program [39], respectively.

C. Straggling parameter

In Fig. 5 we show the normalized energy-loss straggling parameter, $\Omega^2/\Omega_{\mathrm{B}}^2$, of SiO_2, Al_2O_3, and ZrO_2 as a function of the projectile energy per atomic mass unit. Ω_{B}^2 is the Bohr energy-loss straggling parameter, which for a monoatomic target of element j is defined as $\Omega_{\mathrm{B},j}^2 = 4\pi n_j Z_1^2 Z_{2,j}$, where $Z_{2,j}$ and n_j are the atomic number and atomic density of the target, respectively. We have adapted Bragg's rule to evaluate the Bohr straggling parameter of a compound $A_{\alpha_1}B_{\alpha_2}\ldots$ as the weighted sum of its constituent elements,

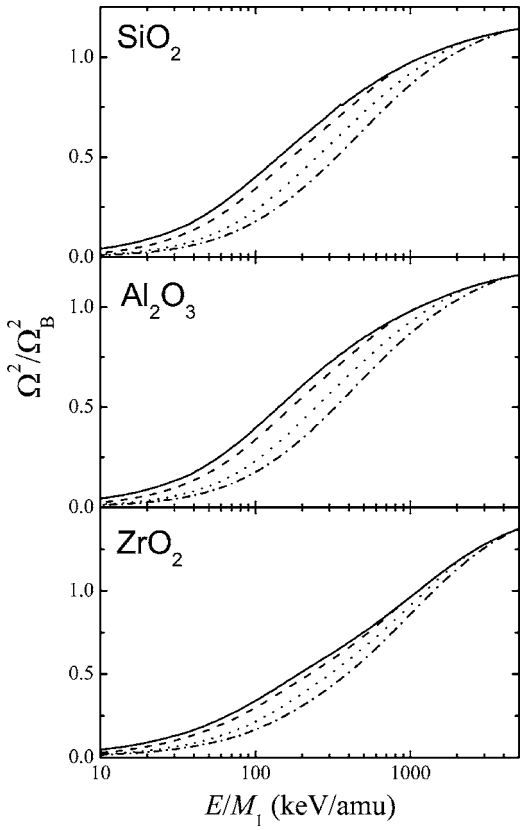

FIG. 5. The normalized energy-loss straggling parameter of SiO_2, Al_2O_3, and ZrO_2 for He (—), Li (--), B (···), and N (-·-) ions as a function of their energy per atomic mass unit.

$$\Omega_B^2 = \mathcal{N} \sum_j \frac{\alpha_j}{n_j} \Omega_{B,j}^2. \tag{21}$$

This expression should be regarded as the high-energy limit of Ω^2. The different curves in Fig. 5 represent our theoretical Ω^2/Ω_B^2 ratios for He, Li, B, and N ions as stated in the figure caption. All calculations were done using the modified BK model for $\rho_q(k)$, Eqs. (10) and (12). The heavier projectiles have a smaller normalized straggling parameter, but all Ω^2/Ω_B^2 curves merge above ~4000 keV/amu. Nevertheless, our results, derived from a more realistic description of the valence-band and inner-shell electrons, show that the Bohr energy-loss straggling of a compound constructed using the adapted Bragg's rule underestimates such high-energy limit by ~15%. This behavior, which can be attributed to the chemical effect, has been recently observed experimentally in the energy-loss straggling of SiO_2 for swift protons [42]. Unfortunately, we are not aware of experimental measurements of Ω^2 for other projectiles to compare with.

IV. CONCLUSIONS

The dielectric formalism has been employed to calculate the electronic stopping power and the energy-loss straggling parameter of SiO_2, Al_2O_3, and ZrO_2 for swift He, Li, B, and N ions. Proper descriptions have been introduced for both the projectile charge density and the target ELF, the former through hydrogenic orbitals or the modified BK model (depending on the number of bound electrons) and the latter using a sum of Mermin-type ELF to describe the single-particle and collective excitations of valence-band electrons and atomic GOSs to account for the ionization of inner-shell electrons. The SCS (proportional to the stopping power) and the straggling parameter were obtained as a weighted sum of all the contributions due to the different charge states that the ion can have inside the target.

Our calculated SCSs reproduce reasonably well the available experimental values in a wide range of projectile energies. The agreement is better when the BK model is used. A plausible explanation for the seemingly poorer success of the hydrogenic model could be the neglect in the present approach of the contributions due to electron capture and loss by the projectile as well as to projectile excitation. We believe that the inclusion of such processes will lead to a substantial improvement in the SCSs predicted by the present method with the ion charge density described using hydrogenic wave functions. On the other hand, there is a lack of measured straggling parameters for He, Li, B, and N ions in the considered oxides. Existing experimental values for protons in SiO_2 seem to indicate a certain increase of Ω^2 around 100 keV/amu, ascribed to the so-called bunching effect [42]. Further theoretical and experimental work is however required to clarify this issue.

ACKNOWLEDGMENTS

This work was supported by the Spanish Comisión Interministerial de Ciencia y Tecnología (BFM2003-04457-C02-01 and BFM2003-04457-C02-02). S.H.A. thanks the Fundación Cajamurcia for financial support and J.M.F.V. expresses his gratitute for a travel grant from the Universitat d'Alacant. The authors thank P. L. Grande for useful discussions.

APPENDIX: GENERALIZED OSCILLATOR STRENGTHS FOR *K*-, *L*- AND *M*-SHELL ELECTRONS

We review in this appendix the formulas for the (nonrelativistic) hydrogenic generalized oscillator strengths (GOS). This information is scattered in several works, see, e.g., Refs. [27,28,43–49]. Many of these references include misprints, and hence our motivation for summarizing here the analytical expressions for these GOSs.

Let us consider a complete atomic shell (n,ℓ) with $N_{n\ell} = 2(2\ell+1)$ electrons. The GOS is usually expressed in terms of the "recoil energy" $Q = \hbar^2 k^2/2m_e$ and energy transfer $W = \hbar\omega$, i.e., $df_{n\ell}(Q,W)/dW$. When dealing with the GOS of one-electron atoms, most authors introduce the reduced variables

$$\mathcal{Q} = \frac{Q}{Z_{2,S}^2 \mathcal{R}} = \frac{\hbar^2 k^2}{2m_e Z_{2,S}^2 \mathcal{R}} \tag{A.1}$$

and

$$\mathcal{W} = \frac{W}{Z_{2,S}^2 \mathcal{R}} = \frac{\hbar\omega}{Z_{2,S}^2 \mathcal{R}}, \tag{A.2}$$

where $\mathcal{R}$ is the Rydberg energy and $Z_{2,S}$ is the effective charge seen by the active electron before ionization takes place, for which we use the effective charge given by Slater's rules [20]. The reduced energy transfer $\mathcal{W}$ is related to the reduced wave number κ of the ionized electron in the final state by

$$\mathcal{W} = \kappa^2 + 1/n^2. \tag{A.3}$$

Then, the GOS of the (n,ℓ) atomic shell is given by

$$\frac{df_{n\ell}(\mathcal{Q},\mathcal{W})}{d\mathcal{W}} = A_n(\mathcal{Q},\mathcal{W}) B_n(\mathcal{Q},\mathcal{W}) C_{n\ell}(\mathcal{Q},\mathcal{W}). \tag{A.4}$$

If $\kappa^2 > 0$, the expressions for A_n and B_n are

$$A_n(\mathcal{Q},\mathcal{W}) = 2^5 (2/n)^3 \mathcal{W} \exp\left[-\frac{2}{\kappa} \times \arctan\left(\frac{2\kappa/n}{\mathcal{Q} - \mathcal{W} + 2/n^2} \right) \right] f_C(\kappa), \tag{A.5}$$

with the Coulomb normalization factor

$$f_C(\kappa) = \left[1 - \exp\left(-\frac{2\pi}{\kappa} \right) \right]^{-1}, \tag{A.6}$$

and

$$B_n(\mathcal{Q},\mathcal{W}) = [(\mathcal{Q} - \mathcal{W})^2 + (2/n)^2 \mathcal{Q}]^{-(2n+1)}. \tag{A.7}$$

But if $\kappa^2 < 0$, A_n should be calculated by means of

$$A_n(\mathcal{Q},\mathcal{W}) = 2^5 (2/n)^3 \mathcal{W} \exp\left[-\frac{1}{\sqrt{-\kappa^2}} \times \ln\left(\frac{\mathcal{Q} - \mathcal{W} + 2/n^2 + 2\sqrt{-\kappa^2}/n}{\mathcal{Q} - \mathcal{W} + 2/n^2 - 2\sqrt{-\kappa^2}/n} \right) \right]. \tag{A.8}$$

Note that A_n and B_n only depend on the principal quantum number n of the considered atomic shell. On the other hand, the coefficients $C_{n\ell}$ depend on both the n and ℓ quantum numbers. Specifically, for the $1s$ shell we have [46] (see also Ref. [27])

$$C_{1s}(\mathcal{Q},\mathcal{W}) = \mathcal{Q} + \frac{\mathcal{W}}{3}. \tag{A.9}$$

For the $2s$, $2p$, $3s$, $3p$, and $3d$ shells

$$C_{n\ell}(\mathcal{Q},\mathcal{W}) = \sum_{j=0}^{j_{\max}} A_j^{(n\ell)}(\mathcal{Q}) (\mathcal{W} - \mathcal{Q})^j, \tag{A.10}$$

where $A_j^{(n\ell)}(\mathcal{Q})$ are polynomials, whose coefficients can be found in Ref. [47]. Notice that our notation is slightly different from that of Sera *et al.* [47]. For instance, we include the factor $(2/n)^3$ in A_n instead of in the $A_j^{(n\ell)}(\mathcal{Q})$ polynomials. Besides, there are a few typographical errors in this reference; the correct expressions for $A_0^{(2p)}$ and $A_3^{(3s)}$ are (in our notation)

$$A_0^{(2p)}(\mathcal{Q}) = \left(\frac{17}{20} + \frac{4}{5}\mathcal{Q} \right) \mathcal{Q}^2 \tag{A.11}$$

and

$$A_3^{(3s)}(\mathcal{Q}) = \left(\frac{256\,768}{6\,200\,145} + \frac{256}{729}\mathcal{Q} \right) \mathcal{Q}^2. \tag{A.12}$$

Converting back to the usual variables Q and W, we finally have for the GOS of the complete shell

$$\frac{df_{n\ell}(Q,W)}{dW} = \frac{1}{Z_{2,S}^2 \mathcal{R}} \frac{df_{n\ell}(\mathcal{Q},\mathcal{W})}{d\mathcal{W}}. \tag{A.13}$$

When atomic units are used, $W = \omega$ and $Q = k^2/2$, so that

$$\frac{df_{n\ell}(k,\omega)}{d\omega} = \frac{df_{n\ell}(Q,W)}{dW}. \tag{A.14}$$

These analytical expressions have been compared to full numerical calculations of the GOS [50] for the Coulomb potential and an excellent agreement is found.

[1] S. A. Campbell, *The Science and Engineering of Microelectronic Fabrication* (Oxford University, Oxford, 1996).

[2] *Interaction of Charged Particles with Solids and Surfaces*, edited by A. Gras-Martí, H. M. Urbassek, N. R. Arista, and F. Flores, NATO ASI Series B: Physics (Plenum, New York, 1991) Vol. 271.

[3] P. Bauer, R. Golser, D. Semrad, P. Maier-Komor, F. Aumayr, and A. Arnau, Nucl. Instrum. Methods Phys. Res. B **136–138**, 103 (1998).

[4] W. N. Lennard, H. Xia, and J. K. Kim, Nucl. Instrum. Methods Phys. Res. B **215**, 297 (2004).

[5] C. Pascual-Izarra, M. Bianconi, G. Lulli, and C. Summonte, Nucl. Instrum. Methods Phys. Res. B **196**, 209 (2002).

[6] C. Pascual-Izarra, M. Bianconi, N. P. Barradas, A. Climent-Font, G. García, J. Gonzalo, and C. N. Afonso, Nucl. Instrum. Methods Phys. Res. B **219–220**, 268 (2004).

[7] Y. Hoshino, T. Okazawa, T. Nishii, T. Nishimura, and Y. Kido, Nucl. Instrum. Methods Phys. Res. B **171**, 409 (2000).

[8] M. Peñalba, J. I. Juaristi, E. Zarate, A. Arnau, and P. Bauer, Phys. Rev. A **64**, 012902 (2001).

[9] I. Abril, R. Garcia-Molina, N. R. Arista, and C. F. Sanz-Navarro, Nucl. Instrum. Methods Phys. Res. B **190**, 89 (2002).

[10] D. A. Thompson and W. D. Mackintosh, J. Appl. Phys. **42**, 3969 (1971).

[11] D. C. Santry and R. D. Werner, Nucl. Instrum. Methods Phys. Res. B **14**, 169 (1986).

[12] T. Gustafsson, E. Garfunkel, D. Starodub, L. Goncharova, S. Sayan, T. Nishimura, and H. Schulte, *Book of Abstracts of CLACSA XI*, 11th Latin American Congress of Surface Science and its Applications (Pucón, Chile, 2003).
[13] E. Bonderup, *Penetration of Charged Particles through Matter* (University of Århus, Århus, 1980).
[14] R. Garcia-Molina, S. Heredia-Avalos, and I. Abril, J. Phys.: Condens. Matter **12**, 5519 (2000); S. Heredia-Avalos, R. Garcia-Molina, and I. Abril, Nucl. Instrum. Methods Phys. Res. B **164–165**, 296 (2000).
[15] S. Heredia-Avalos and R. Garcia-Molina, Nucl. Instrum. Methods Phys. Res. B **193**, 15 (2002).
[16] G. Schiwietz, and P. L. Grande, Nucl. Instrum. Methods Phys. Res. B **175–177**, 125 (2001); G. Schiwietz, K. Czerski, M. Roth, F. Staufenbiel, and P. L. Grande, Nucl. Instrum. Methods Phys. Res. B **225**, 4 (2004); **226**, 683 (2004).
[17] P. L. Grande (private communication).
[18] W. Brandt and M. Kitagawa, Phys. Rev. B **25**, 5631 (1982).
[19] W. Brandt, Nucl. Instrum. Methods Phys. Res. **194**, 13 (1982).
[20] J. C. Slater, Phys. Rev. **36**, 57 (1930).
[21] N. D. Mermin, Phys. Rev. B **1**, 2362 (1970).
[22] I. Abril, R. Garcia-Molina, and N. R. Arista, Nucl. Instrum. Methods Phys. Res. B **90**, 72 (1994).
[23] D. J. Planes, R. Garcia-Molina, I. Abril, and N. R. Arista, J. Electron Spectrosc. Relat. Phenom. **82**, 23 (1996).
[24] I. Abril, R. Garcia-Molina, C. D. Denton, F. J. Pérez-Pérez, and N. R. Arista, Phys. Rev. A **58**, 357 (1998).
[25] H. Bethe, Ann. Phys. **5**, 325 (1930).
[26] U. Fano, Annu. Rev. Nucl. Sci. **13**, 1 (1963).
[27] R. F. Egerton, *Electron Energy-Loss Spectroscopy in the Electron Microscope* (Plenum Press, New York, 1989).
[28] M. A. Kumakhov and F. F. Komarov, *Radiation from Charged Particles in Solids* (American Institute of Physics, New York, 1989).
[29] J. C. Moreno-Marín, I. Abril, and R. Garcia-Molina, Nucl. Instrum. Methods Phys. Res. B **193**, 30 (2002).
[30] J. F. Ziegler and J. P. Biersack, *SRIM-2003. The Stopping and Range of Ions in Matter*, Version 2003. 18–20, code available from http://www.srim.org
[31] B. L. Henke, E. M. Gullikson, and J. C. Davis, At. Data Nucl. Data Tables **54**, 181 (1993). The ASCII files for the f_1 and f_2 scattering factors of the different elements can be obtained from http://xray.uu.se/hypertext/henke.html
[32] H. R. Philipp, in *Handbook of Optical Constants of Solids*, edited by E. D. Palik (Academic Press, Orlando, 1985), Vol. I, p. 749.
[33] C. J. Powell, in *Handbook of Optical Constants of Solids*, edited by E. D. Palik (Academic Press, Orlando, 1985), Vol. I.
[34] H.-J. Hagemann, E. Gudat, and C. Kunz, Deutsches Elektronen-Synchroton Report No. DESY SR-74/7, Hamburg, 1974 (unpublished); J. Opt. Soc. Am. **65**, 742 (1975).
[35] J. Frandon, B. Brousseau, and F. Pradal, Phys. Status Solidi B **98**, 379 (1980).
[36] E. Shiles, T. Sasaki, M. Inokuti, and D. Y. Smith, Phys. Rev. B **22**, 1612 (1980).
[37] ICRU, *Stopping Powers and Ranges for Protons and Alpha Particles* (ICRU, International Commission on Radiation Units and Measurements, Bethesda, Maryland, 1994), Vol. 49.
[38] W. H. Bragg and R. Kleeman, Philos. Mag. **10**, 318 (1905).
[39] G. Schiwietz and P. L. Grande, Nucl. Instrum. Methods Phys. Res. B **153**, 1 (1999).
[40] A. Arnau, M. Peñalba, P. M. Echenique, F. Flores, and R. H. Ritchie, Phys. Rev. Lett. **65**, 1024 (1990).
[41] A. Sharma, A. Fettouchi, A. Schinner, and P. Sigmund, Nucl. Instrum. Methods Phys. Res. B **218**, 19 (2004).
[42] J. H. R. dos Santos, P. L. Grande, M. Behar, J. F. Dias, N. R. Arista, J. C. Eckardt, and G. H. Lantschner, Phys. Rev. A **68**, 042903 (2003).
[43] M. C. Walske, Phys. Rev. **101**, 940 (1956).
[44] B. H. Choi, Phys. Rev. A **7**, 2056 (1973).
[45] D. H. Madison and E. Merzbacher, in *Theory of Charged-Particle Excitation, Atomic Inner-Shell Processes*, edited by B. Crasemann (Academic Press, New York, 1975) Vol. I, p. 1.
[46] K. Sera, K. Ishii, M. Kamiya, A. Kuwako, and S. Morita, Phys. Rev. A **21**, 1412 (1980).
[47] K. Sera, K. Ishii, A. Yamadera, A. Kuwako, M. Kamiya, M. Sebata, S. Morita, and T. C. Chu, Phys. Rev. A **22**, 2536 (1980).
[48] F. Bell, J. Chem. Phys. **85**, 303 (1986).
[49] Z. Liu and J. Cipolla, Comput. Phys. Commun. **97**, 315 (1996).
[50] S. Segui, M. Dingfelder, J. M. Fernández-Varea, and F. Salvat, J. Phys. B **35**, 33 (2002).